The characterization of x-ray photocathodes in the 0.1–10-keV photon energy region

B.L. Henke, J. P. Knauer,[a] and K. Premaratne
University of Hawaii, Honolulu, Hawaii 96822

(Received 25 September 1980; accepted for publication 2 December 1980)

A method and an instrument are described for the measurement of the absolute quantum yield for front-surface and transmission photocathodes in the 0.1–10-keV photon energy region. The total and the secondary electron photoemission yields have been measured for the Al, Au, CuI, and CsI photocathodes as required for the absolute calibration of the x-ray diode detectors and for the x-ray streak cameras. The relative secondary electron yields have also been measured for the same photocathodes by high resolution electron spectroscopy of the secondary electron energy distributions, which are in good agreement with the absolute yield measurements. The secondary electron yield of CsI is ten to one-hundred times higher than that for Au in the 0.1–10-keV region and with a secondary energy distribution that is appreciably sharper. For these reasons, CsI should be an effective photocathode for sensitive, time-resolved spectroscopy into the picosecond region. It is verified experimentally that the secondary electron quantum yield varies approximately as $E\mu(E)$, with E as the photon energy and $\mu(E)$ as the photoionization cross section, and that the primary (fast) electron quantum yield is a small fraction of the total yield and varies approximately as $E^{-2}\mu(E)$. A simple model for x-ray photoemission is described which leads to semiempirical equations for front- and back-surface secondary electron photoemission as based upon an escape depth parameter that may be obtained from yield-versus-photocathode thickness data. The model predictions are in good agreement with experiment.

PACS numbers: 79.60.Cn, 79.60.Eq, 72.10. – d

I. INTRODUCTION

Time-resolved x-ray spectroscopy has become of considerable importance in the temperature density composition diagnostics of high-temperature plasmas involved in controlled thermonuclear fusion studies which utilize laser, particle beam, or magnetic compression-confinement production. The time duration of the associated x-ray emission ranges from picoseconds to seconds. Time-resolved x-ray spectroscopy is also important in the development of superradiant, pulsed x-ray sources, their application to studies of the radiation effects of x-ray bursts upon materials, and the x-ray analysis of atomic, molecular, and solid-state time-resolved processes into the picosecond region.

The electron currents that are emitted by photocathodes under x-ray excitation can be a very effective basis for time resolved spectroscopic measurement using x-ray diode or streak camera detection.[1–5] In the latter, an x-ray spectrum can be established along a slit-defined transmission photocathode of the streak camera by using focussing filter-total-reflection monochromator, crystal/multilayer arrays, or nonfocussing, Bragg reflecting crystal/multilayer analyzer systems.

In time-resolved x-ray spectroscopy, the ultimate limit on the achievable time resolution is the quantum conversion efficiency of the photocathode (which determines signal statistics) and the energy spread of the emitted electrons as is noted in Fig. 1 (which determines the time resolution).[6] The relatively small fraction of fast electrons that is photoemitted is effectively blocked by the electron optical apertures of the typical streak camera. In Fig. 2 the difference in the arrival time at the output end of the streak camera is given as a function of the energy width Δ of the secondary electron energy distribution, the extraction field ϵ_0, and of the geometry of the camera. In addition to the absolute yield-versus-photon energy and the shape of the secondary electron distribution curves, other important characteristics of the x-ray photocathode are its stability, reproducibility, simplicity of spectral response, and the linearity of its time response. Described here is a method and an instrument for the measurement of the absolute total and secondary electron yields

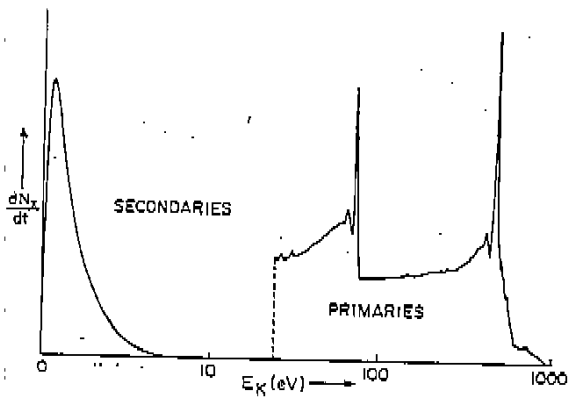

FIG. 1. In the 0.1-10-keV photon energy region the larger fraction of the electrons that are emitted are the secondary electrons, typically as a narrow distribution below 10 eV. The higher energy, fast electron photoemission consists of relatively sharp elastically scattered photoelectrons and Auger electron "lines" along with a much larger number of inelastically scattered electrons in their low-energy tail region.

[a]Present address: Lockheed, LMSC Palo Alto Research Laboratory, Org. 52-11, Building 203, 3251 Hanover Street, Palo Alto, California 94304.

 0021-8979/81/1509-12$01.10

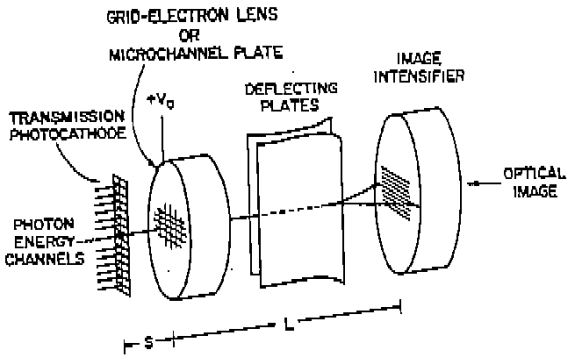

TEMPORAL RESOLUTION LIMIT, τ

$$\tau = 3.37\ \frac{(\Delta)^{1/2}}{\epsilon_0}\left\{1+\frac{1}{4}\left(\frac{L}{S}-2\right)\left(\frac{\Delta}{eV_0}\right)^{1/2}\ldots\right\}\ \text{PICOSECONDS}$$

Δ – SECONDARY ELECTRON ENERGY SPREAD IN eV

ϵ_0 = EXTRACTION FIELD, V_0/S IN kV/mm

FIG. 2. Schematic of an x-ray streak camera for time-resolved x-ray spectroscopy. Its ultimate time resolution is determined by the difference in arrival time τ at the output end of the camera associated with the energy width Δ of the secondary electron distribution emitted from the transmission photocathode. For a secondary electron energy spread Δ of 2 eV and an extraction field ϵ_0 of 5 kV/mm, the time resolution τ is approximately 1 ps. (The fast electron photoemission is essentially blocked electron optically in the streak camera.)

(electrons emitted per normally incident photon) for both front-surface and transmission photocathodes in the 0.1–10-keV photon energy region and the application to the characterization of photocathode materials of current practical importance such as gold and cesium iodide. In addition to the measurements of the total electron emission in the secondary and primary electron components, high-resolution electron spectroscopic measurements of the secondary electron energy distributions for these photocathodes are also presented. A simple model for the quantum yield of x-ray photoemission is outlined here that includes the effect of photocathode thickness upon the front- and back-surface emissions.

II. THE MEASUREMENT OF X-RAY PHOTOEMISSION

The facility that has been developed for making absolute yield measurements in the photon energy region of 0.1–10 keV is shown in Fig. 3. Six filtered fluorescent sources of essentially monochromatic characteristic x radiations may be excited by a closely coupled, 2–4 kW demountable x-ray source of strong characteristic line radiation of photon energy just above that of the fluorescent line being used.[7] The photocathodes are also brought in as closely as possible to the fluorescent source in order to maximize the photoemission currents to be measured. The absolute x-ray flux per stearadian at the same take-off angle from a 3-cm fluorescent source disk is measured by a calibrated flow proportional counter at the end of an extended vacuum path and with an accurately defined pinhole aperture (to limit the counting rates to less than ~5000 c/s for negligible coincidence loss).

An eight-position, front-surface photocathode Teflon sample holder (four positions for transmission photocathodes) has been accomodated in order to allow precise relative measurement, for example, of a series of different photocathode materials, or of different photocathode thicknesses.

A cylindrical "grid" technique has been developed for the retarding of the secondary electron emission current in the determination of the primary or fast electron components. This cylindrical grid system is so designed that *no* direct x-radiation can reach surfaces that can contribute background emission currents which might return to the photocathode when it is at a relatively positive, retarding potential. High transparency mesh surfaces are placed in front of surfaces which are at appeciably higher positive potential, thereby trapping the large angle photoemitted electrons which might otherwise excite secondary electron background. This cylindrical grid method for separating the secondary from the total photoemission current is illustrated as applied to both front-surface and transmission photocathode characterizations in Figs. 4, 5, 6, and 7. As illustrated here, detailed equipotential maps of the accelerating and retarding fields have been compared along with photoemitted electron ray traces[8] in order to determine the potential "hill" characteristics of the cylindrical grids.

The filter-window material on the proportional counter aperture is identical to that on the entrance aperture to the photocathode section so that their transmissions cancel in the absolute yield measurements. By using a similar material on the back, substrate surface of the transmission photocathodes, the back-surface photoemission current is effectively cancelled by that from the adjacent entrance window surface (0.8-cm separation) thereby improving the measurement statistics in the difference measurements.

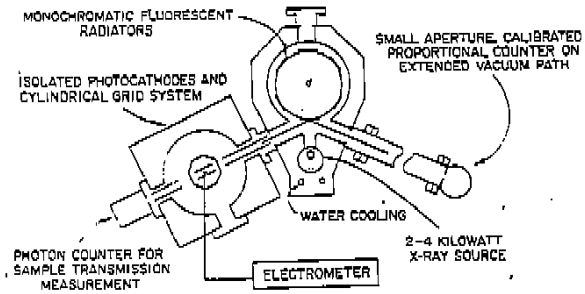

FIG. 3. Instrument for the relative and absolute measurement of the quantum yields for front-surface and transmission photocathodes in the 0.1–10-keV photon energy region. Characteristic fluorescent line sources are excited by a closely coupled x-ray source of strong line radiation of photon energy just above that of the fluorescent lines. The fluorescent line intensities are measured by a calibrated proportional counter which views the source at the same take-off angle as does the photocathode. The filter material between the source and the photocathode is identical to that on the proportional counter aperture. The monochromaticity of the fluorescent sources under similar excitation and filtering are evaluated spectroscopically and are monitored by a multichannel pulse height analyzer during the measurements. The electrometer current output is converted proportionally to a frequency from 0 to 25 kHz for rapid and precise digital signal averaging.

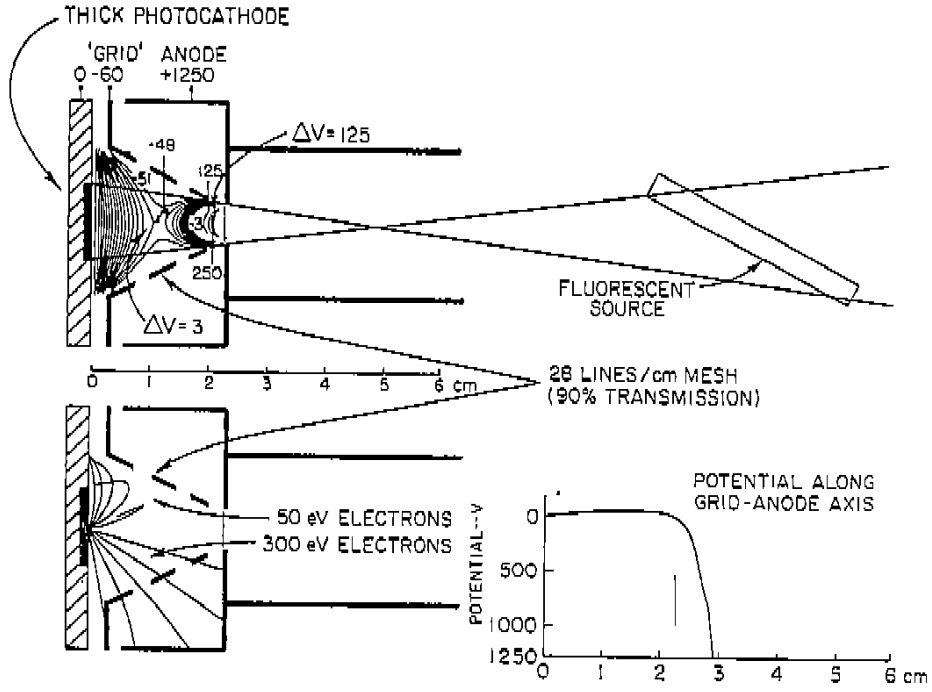

FIG. 4. Cylindrical grid geometry for front-surface photoemission measurement. Illustrating the retarding field, potential hill characteristics and electron ray traces for the measurement of the fast electron photoemission component.

The x-radiation that passes through the side-window proportional counter is limited by the entrance pinhole window to a narrow beam that just misses the central anode wire and, if not absorbed, proceeds through an exit hole in the opposite side and into a positive potential electron trap region. The effective absorption path between the two apertures is 3.51 cm. The anode wire diameter is 50 μ. When possible, the photon absorption efficiency is set between 85 and 95% for a given photon energy by the choice of the counter gas and its pressure. This "pressure tuning" minimizes ionization charge loss at the entrance window and photon loss through the exit aperture and provides minimum-width pulse height distributions.[7] A multichannel pulse height analyzer is used to monitor the output pulses of the proportional counter in order to verify that a given fluorescent line source is optimally excited and filtered for

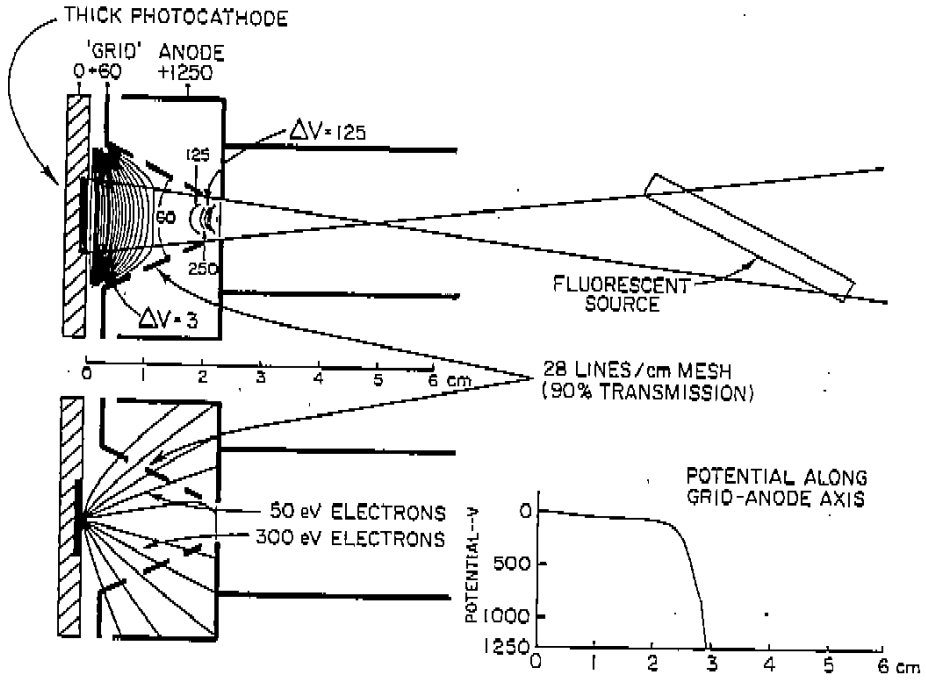

FIG. 5. Total yield measurement of front-surface photoemission.

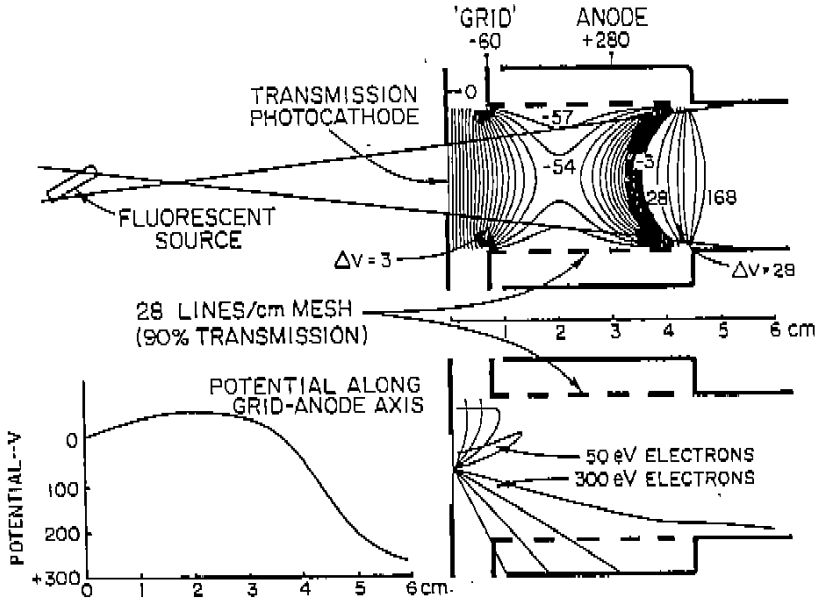

FIG. 6. Cylindrical grid geometry for back surface photoemission measurement. Illustrating the retarding field, potential hill characteristics and electron ray traces for the measurement of the fast electron photoemission component.

minimum background x-radiation.

In Table I are presented a list of the fluorescent line sources that were employed in the measurements that are reported here along with a description of the excitation, filtering, and flow proportional counter parameters that were chosen to obtain the calibrated photon excitation to the photocathodes.

The photocathode materials were vacuum evaporated upon chromium-coated microscope slide substrates and were mounted upon a rotatable, insulating Teflon structure. The vibrating reed preamplifier head of a Carey 401 Electrometer was connected through a rigid coaxial section to a low-loss feedthrough and to a spring contact upon a polished button which fastens each photocathode to the holder. Typical measurement current levels for these studies were between 10^{-12} and 10^{-15} A. A mechanical shutter for the x-ray beam was provided between the source and the photocathode to permit a determination of the effective background current ($\sim 10^{-17}$ A).

For rapid and convenient signal averaging, the electrometer output current was converted by a variable frequency oscillator circuit (IC-Raytheon 4151) to a frequency that is precisely proportional to the current and in the 0–25-kHz region. The quantum yield (as the charge collected per photon incident upon the photocathode) is measured by counting the number of cycles within a time interval that is determined by that required to collect a set number of photons at the proportional counter (typically 10 000 counts).

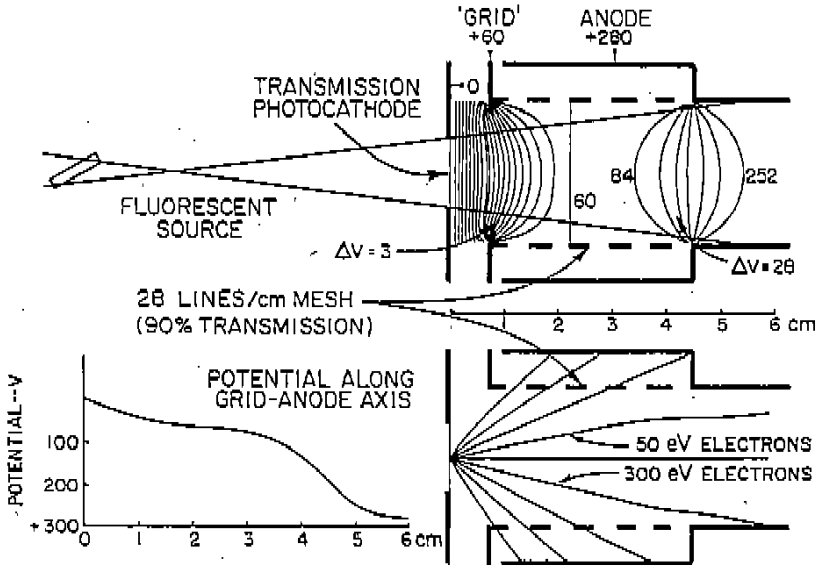

FIG. 7. Total yield measurement of back-surface photoemission.

TABLE I. Parameters for the calibrated fluorescent line excitation sources.

λ (Å)	E (eV)	Fluorescent source	Exciting source	Filter	Filter thickness	Filter transmission (%)	Proportional counter		
							Gas	Pressure	Efficiency (%)
1.79	7469	Ni-Kα	Cu-K	Ni	12 μ	47	P-10	760	53
1.94	6397	Fe-Kα	Cu-K	Ni	12 μ	38	P-10	760	69
2.29	5411	Cr-Kα	Cu-K	Ni	12 μ	20	P-10	760	84
4.16	2981	Ag-Lα	Cr-K	Ag	0.5 μ	77	P-10	760	85
5.41	2292	Mo-Lα	Cr-K	Ag	0.5 μ	59	P-10	760	85
7.13	1739	Si-Kα	Cr-K	Ag	0.5 μ	35	P-10	760	98
8.34	1486	Al-Kα	Cr-K	Ag	0.5 μ	22	P-10	760	100
9.89	1254	Mg-Kα	Al-K	Mg	6.6 μ	57	Propane	200	80
13.3	930	Cu-Lα	Al-K	MG	6.6 μ	28	Propane	200	98
14.6	852	Ni-Lα	Al-K	Mg	6.6 μ	20	Propane	200	99
17.6	705	Fe-Lα	Ni-L	Fe	0.6 μ	36	Propane	75	95
18.3	677	F-Kα	Ni-L	Fe	0.6 μ	33	Propane	75	96
23.6	525	O-Kα	Ni-L	Formvar	52 μg/cm^2	66	Propane	50	99
31.6	392	N-Kα	Cu-L, O-K*	Formvar	52 μg/cm^2	43	Propane	50	100
44.7	277	C-Kα	Cu-L, O-K*	Formvar	52 μg/cm^2	84	Propane	100	82
64.4	193	Mo-Mζ	C-K	Formvar	52 μg/cm^2	65	Propane	50	88
82.1	151	Zr-Mζ	C-K	Formvar	52 μg/cm^2	46	Propane	50	98
114	109	Be-Kα	C-K	Formvar	52 μg/cm^2	20	Propane	50	100

*Oxidized copper anode.

III. EXPERIMENTAL RESULTS

A. Front-surface photoemission—thick photocathodes

For x-ray diode detectors, effective front-surface emission photocathodes have been aluminum, gold, the semiconductor copper iodide, and the insulator cesium iodide. These have been included in this study. The materials, vacuum evaporated as thick photocathode systems upon chromium-coated microscope slide substrates, were handled in a dry-nitrogen atmosphere outside the vacuum systems. The total yields and the fast, primary electron yields (secondary electrons retarded by a -50-V potential "hill") were measured for eighteen photon energies in the 0.1- to 10-keV region. The total yield data are presented in Figs. 8, 9, 10, and 11. In Fig. 12 are presented the associated curves for the measured ratios of the primary yield (fast electron component) to the total yield, Y_p/Y_T. From these data it may be noted that the dominant photoemission current is that of the secondary electrons, and that for the several photocathodes characterized here, the primary yield are very similar and the insulator and semiconductor photocathodes, CsI and CuI, have considerably higher secondary electron yields than do the metal photocathodes Al and Au.

It is of interest to compare here the secondary electron energy distributions for these same photocathodes. To measure these, the photocathodes were transferred to an electron spectrograph and analyzed with at about 0.01-eV resolution as has been described previously.[9,10] Presented in Figs. 13 and 14 are spectra for the four photocathodes as photoexcited by C-Kα (227 eV) and Cu–Kα (8080 eV). The peak intensities of the distributions are given relative to that for the gold photocathode. Also noted here are the peak positions E_{KP} and the full width at half maximum Δ for each secondary electron energy distribution.

It is important to note that, as is illustrated here, there is no significant change in the shape of the secondary electron energy distributions for a given photocathode in the 0.1–10-keV excitation region. It is also of considerable practical importance that the CuI and CsI photocathodes do have the narrow secondary electron energy distributions and high quantum efficiency that is required for sensitive time-resolved spectroscopy in the picosecond range[11] (see Fig. 2).

By measuring the area under the secondary electron energy distribution curves, as those presented in Figs. 13 and 14, we have obtained the relative secondary electron yields for photocathodes as excited and analyzed under identical conditions. In Table II are presented the secondary electron

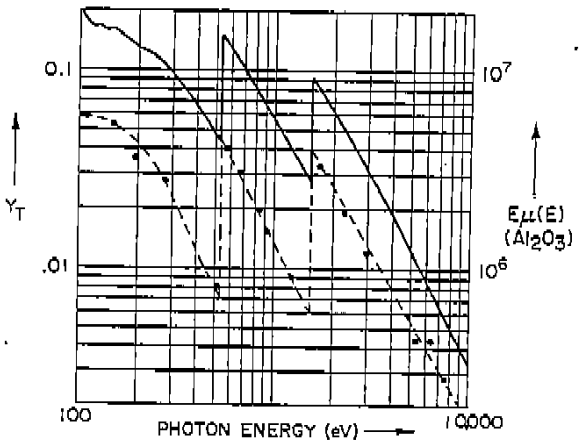

FIG. 8. Front-surface, total quantum yield for a 1400-Å evaporated aluminum photocathode. [Compared to $E\mu(E)$ for Al_2O_3.]

TABLE II. Y_S(CsI)/Y_S(Au) for thick photocathode secondary electron yields. Relative Yields—Y_s(CsI)/Y_s(Au).

Photon energy (eV)	From absolute yield	From secondary electron energy distributions
277	11	10
1487	44	42
8080	34	34

B. Back-surface photoemission—transmission photocathodes

Gold and cesium iodide transmission photocathodes are currently being applied in x-ray streak cameras for time-resolved spectroscopy into the picosecond range.[11] We have presented the back-surface secondary electron emission yield-versus-photon energy data for the 0.1–10-keV region for these photocathodes in Figs. 16 and 17. The transmission photocathode films were of about 250- and 1000-Å thickness, respectively, and were vacuum evaporated upon carbon foil substrates of about 50 μg per cm^2 mass thickness. The x-ray transmissions of the substrate carbon foils were measured and these values were used to obtain the secondary electron yield per normally incident photon as transmitted to the front surface of the photocathode film. Carbon foil substrates were chosen because these have good mechanical strength, low attenuation for the low-energy x-rays, and are conducting. Because of the very low photoemission efficiency of the carbon substrates, it is expected that these yield data are essentially independent of the substrate contribution and would be the same for the equivalent self-supporting film system.

In Figs. 18 and 19 are presented the back-surface yield-versus-photocathode film thickness for the gold and cesium iodide systems. Because of the very broad maxima characteristic of the yield-versus-thickness curves for the transmission photocathodes, we have chosen the thicknesses of 250 and 1000 Å as appropriate for the Au and CsI transmission photocathodes, which allow somewhat greater uniformity and strength without a serious decrease in yield from an optimum value for the low-energy x-rays.

IV. A SIMPLE MODEL FOR FRONT- AND BACK-SURFACE X-RAY PHOTOEMISSION YIELDS AND FOR THE EFFECT OF PHOTOCATHODE THICKNESS: COMPARISON WITH EXPERIMENTAL RESULTS

In a previous work[10] we presented a detailed phenomenological model for x-ray photoemission for thick photocathodes. Here we extend this description to include the effect of photocathode thickness for the thin metal or insulator photocathode for which both front- and back-surface photoemission are excited by incident x radiation.

We had noted that the x-radiation energy that is deposited within the photocathode is converted through photoelectric absorption to that of photoelectrons and subsequently to emitted Auger electrons and fluorescent radiation. Nearly all of this deposited energy is transformed to that of primary electrons within the photocathode except for a small fraction that is associated with the primaries and fluorescence that escapes through the photocathode surface. The energy of these internal primaries is initially and completely transformed to the excitation energy of secondary electrons (mostly by promoting valence-band electrons to the conduction band and by the deexcitation of excited plasmons). Heuristically we can relate the number of secondaries N that are excited within a unit photocathode area of effective escape depth λ_S in a thick photocathode to the x-radiation energy deposited by the expression

$$N\bar{E}_{KS} \simeq I_0 \rho E \mu(E) \lambda_S, \tag{1}$$

where $\bar{E}_{KS}$ is the mean energy of the excited secondaries, I_0 is the number of photons per unit area normally incident and

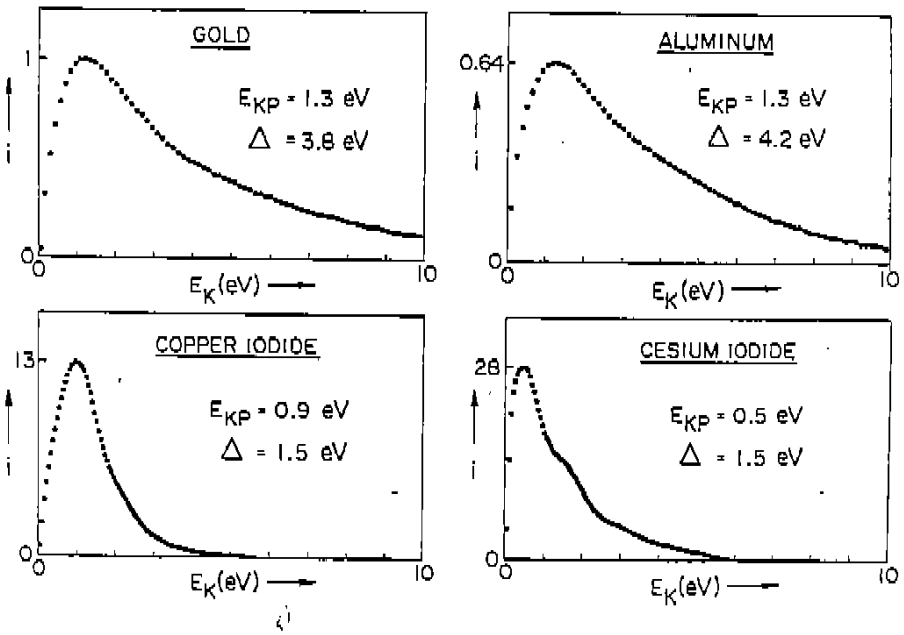

FIG. 13. Secondary electron energy distributions for Au, Al, CuI, and CsI photocathodes (as measured in Figs. 8–11). Excited by C-Kα (277 eV) x radiation.

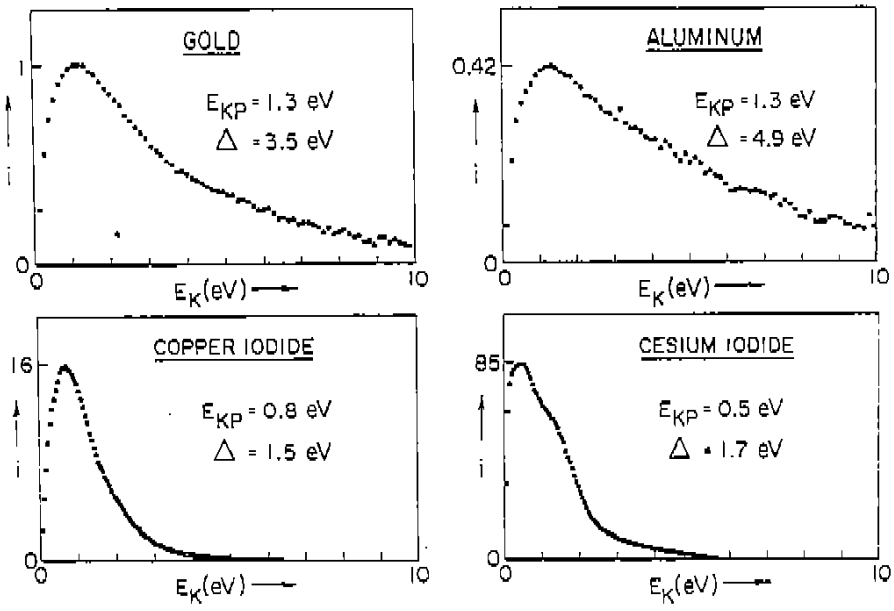

FIG. 14. Secondary electron energy distributions of Au, Al, CuI, and CsI photocathodes (as measured in Figs. 8–11). Excited by Cu-Kα (8080 eV) x radiation. Note that the shapes of these distribution curves are essentially the same as those excited by the C-Kα (277 eV) x radiation.

of energy E, $\mu(E)$ is the mass photoionization cross section, and ρ is the mass density. Assuming that the number of secondaries emitted per incident photon (the yield, Y_S for a thick photocathode) is simply proportional to that number of internally excited secondaries within the escape volume, we may then predict that

$$Y_S \sim \rho E \mu(E) \lambda_S / \bar{E}_{KS}. \tag{2}$$

We have not been able to detect any significant change in the energy distribution of the emitted secondary electrons with photon energy in the 0.1–10-keV region as is illustrated here in Figs. 13 and 14. This implies that the internal energy distributions are also independent of the x-ray photon energy and that $\bar{E}_{KS}$ is a constant for a given photocathode material. We may therefore predict for the yield of secondary electrons from a thick photocathode the relation

$$Y_S = K_S \rho E \mu(E) \lambda_S. \tag{3}$$

Applying the same reasoning for the emission of the primary electrons, we note that $\bar{E}_{KP}$ for the internal distribution of primaries would be essentially proportional to the incident photon energy E, and we obtain from a relation analogous to Eq. (2),

$$Y_P = K_P \rho \mu(E) \lambda_P. \tag{4}$$

Because λ_S the escape length for secondaries is independent of the photon energy, the secondary electron yield dependence upon the x-ray photon E should be approximately as $E\mu(E)$. This is confirmed by a comparison of the $E\mu(E)$ curves that are presented along with the log-log plots of the experimental yield data in Figs. 8–11. (The total yield plotted in these figures is mostly that of secondary electron emission.)

An escape depth for the primaries which are emitted into the sharp, elastically scattered photoelectron and Auger electron lines (as depicted in Fig. 1) may be a mean free path, and, for the kilovolt region, may depend upon the energy[9,12,13] as approximately $E_K^{0.8}$. However the total primary yield that is measured here, Y_P, is mostly that of the fast electrons which have suffered many inelastic collisions before escaping (into the low-energy tails of the line spectra as illustrated in Fig. 1) and for these, the effective escape depth λ_P is more accurately described as a practical range. Its energy dependence, therefore, might be obtained for the kilovolt region by a logarithmic extrapolation of the Bethe-Bloch continuous-slowing-down-approximation range given in the tables of Pages et al. as approximately the relation λ_P (CSPA) $= R_0 E_K^{1.9}$.[14,15] We may thus predict then since the primary energies should increase as the photon energy, the primary yield Y_P depends upon photon energy as approximately $E^{1.9}\mu(E)$. It then follows from Eqs. (3) and (4) that the ratio Y_P/Y_S should depend upon the x-ray photon energy in the kilovolt region as approximately $E^{0.9}$. This dependence is suggested by the experimental data for Y_P/Y_T presented in Fig. 12 ($Y_P/Y_T = Y_P/(Y_S + Y_P) \simeq Y_P/Y_S$, for $Y_P \ll Y_S$).

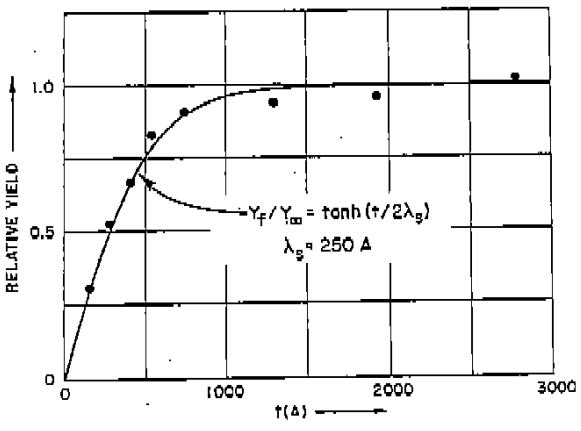

FIG. 15. Front-surface secondary electron yield for CsI vs photocathode film thickness and fit according to a yield equation predicted by the x-ray photoemission model presented here. (The CsI was evaporated upon a chromium substrate of relatively very low photoemission efficiency.)

In the detailed analysis of secondary electron photoemission that is presented in Ref. 10 are predicted this photon energy dependence through the factor $E\mu(E)$ and also the secondary electron energy distributions for photoemission from metals, semiconductors, and insulators for *thick* photocathodes. As in Kane's secondary electron transport model,[16] we have assumed in this analysis that an electron-electron collision will drop the energy of a random-walking secondary electron to below the vacuum level and hence eliminate it from the group of electrons that may escape from the photocathode surface. Following Kane's notation, we define the linear scattering cross section (inverse mean free path) for electron-electron collisions as b. The electron-phonon collision cross section is defined as a for which the associated energy loss per collision is very small. For a given photocathode, a and b are assumed to be constants. In Ref. 10, we have used Kane's transport model to predict an isotropic distribution of secondaries just inside the photocathode surface and have then applied the usual escape cone integral over all the secondary energies to determine the secondary electron energy distribution and yield as emitted from the photocathode surface. In this model we neglected any enhancement of the secondary emission resulting from a reflection of those secondaries that are outside the escape cone (into the photocathode and possibly "wandering" back by a random walk to the surface and escaping). For metals, any reflecting secondaries would most likely suffer an electron-electron collision ($b \gg a$) in order to return and would thereby be dropped to below the vacuum level. For insulators, for which electron-electron collisions are unlikely ($b \ll a$), it is suggested in Ref. 10 that the internal reflection of secondaries may contribute to a small enhancement of photoemission. This enhancement factor, however, is independent of photon energy and thus is essentially constant for a given photocathode.

As outlined in the Appendix, we have applied a similar analysis for the case of *thin* photocathodes for which both front- and back-surface photoemission is involved as illustrated in Fig. 20. We have simply placed a limit of t for the thickness of the photocathode instead of infinity as in Kane's original analysis for a semi-infinite photocathode and as has been done by Pong et al.[17] for a finite photocathode. We neglect any contributions to the yield from the front- or back-surface reflections because it can be shown that such are significant only if the photocathode thickness approaches a value equal to the escape length λ_s. As will be shown in the following, a practical thickness for the x-ray photocathode will be several times greater than this escape length value. In addition to our considering enchancement of emission resulting from internal reflections to be small and constant, we have also considered the mean attenuation length for the photons within the photocathode, $(\mu\rho)^{-1}$, to be very large as compared with the mean free paths b^{-1} and a^{-1}.

This simple extension of our x-ray photoemission model results in the following relations for the secondary electron emission yields for the front and back surfaces Y_f and Y_b as a function of the photocathode thickness t: front surface,

$$Y_f = K\rho E\mu(E)\left(\frac{c}{u(u+c)}\right)\left(\frac{1-e^{-ut}}{1+\delta e^{-ut}}\right), \tag{5}$$

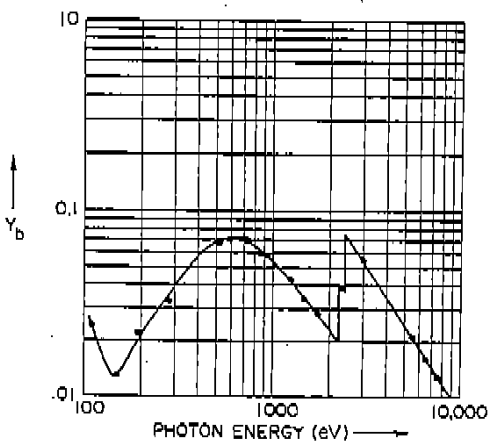

FIG. 16. Back-surface secondary electron quantum yield for a 230-Å Au transmission photocathode.

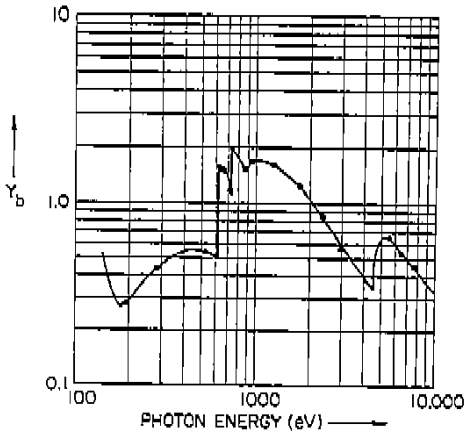

FIG. 17. Back-surface secondary electron quantum yield for a 1020-Å CsI transmission photocathode.

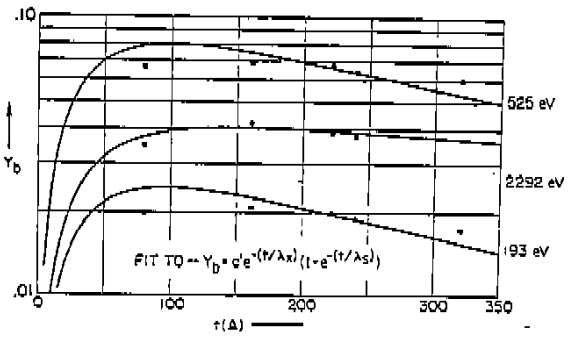

FIG. 18. Back-surface secondary electron yield for Au-vs-transmission photocathode film thickness and fit according to a yield equation predicated by the x-ray photoemission model presented here.

back surface,

$$Y_b = K\rho E\mu(E)\left(\frac{ce^{-\mu\rho t}}{u(u+c)}\right)\left(\frac{1-e^{-ut}}{1+\delta e^{-ut}}\right). \quad (6)$$

Here, as functions of the linear cross sections for electron-phonon and electron-electron scattering, a and b, we have introduced the parameters:

$$c = (a+b)$$
$$u = (c^2 - ac)^{1/2} = (b^2 + ab)^{1/2},$$
$$\delta = (c-u)/(c+u).$$

K is a material constant which depends upon the electronic constants of the photocathode material as the band-gap energy E_G and the electron affinity E_A for insulators, and upon the Fermi energy E_F and the work function W for metals (as discussed in Ref. 10).

As shown in Kane's one-dimensional random-walk analysis for secondary electron transport to the surface, u^{-1} is the escape length for a photocathode of infinite thickness and defined here as an average escape length, λ_S measured normal to the surface. (The mean free paths for electron-phonon and electron-electron scattering, a^{-1} and b^{-1}, as adopted here from Kane's one-dimensional random-walk analysis, are the averages of the projections along the direction normal to the photocathode surface of the actual three-dimensional random-walk scattering path segments. These one-dimensional mean free paths have been shown by exact three dimensional random-walk analyses to be approximately one-half the magnitude of the corresponding actual mean free paths.[10])

For *insulators*, $b \ll a$, and therefore $u \approx (ab)^{1/2}$ and $\delta \approx 1$. Defining an escape length λ_S as equal to $(ab)^{-1/2}$ for insulators, we obtain from Eqs. (5) and (6)

$$Y_f = K\rho E\mu(E)\lambda_S \tanh(t/2\lambda_S) \quad (7)$$

and

$$Y_b = K\rho E\mu(E)e^{-(t/\lambda_x)}\lambda_S \tanh(t/2\lambda_S). \quad (8)$$

For *metals*, $b \gg a$, and therefore $c \approx b$, $u \approx b$, and $\delta \approx 0$. Defining an escape length λ_S for metals to be equal to b^{-1}, we may obtain from Eqs. (5) and (6)

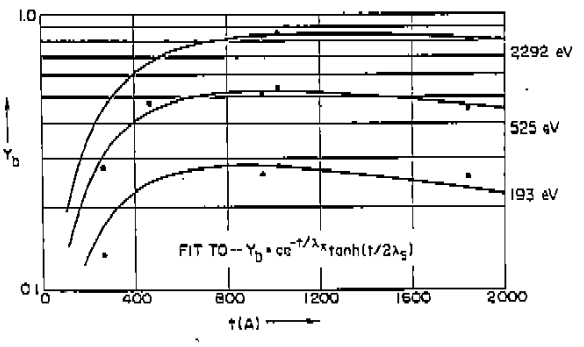

FIG. 19. Back-surface secondary electron yield for CsI-vs-transmission photocathode thickness and fit according to a yield equation predicted by the x-ray photoemission model presented here.

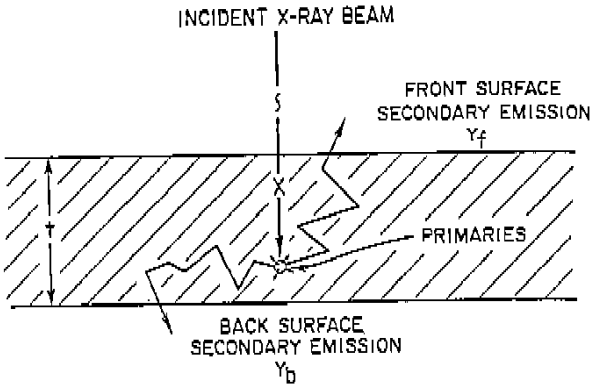

FIG. 20 Front- and back-surface emission geometry for the transmission photocathode.

$$Y_f = K'\rho E\mu(E)\lambda_S(1 - e^{-t/\lambda_S}) \quad (9)$$

and

$$Y_b = K'\rho E\mu(E)\lambda_S e^{-t/\lambda_x}(1 - e^{-t/\lambda_S}). \quad (10)$$

Here λ_x is the x-ray attenuation length, $(\mu\rho)^{-1}$.

In Fig. 15 is shown a fit of Eq. (7) to the experimental data of yield-versus-thickness for the insulator, cesium iodide on a chromium-coated substrate. Beacuse the trend of the experimental data is to pass through the origin and because the yield at 277 eV for chromium is very small as compared with that of CsI (about 3%), it is suggested that the substrate contributes a relatively small effect upon these yield data. The best fit parameter λ_S equal to 250 Å, is in good agreement with the measurements of the escape length for secondary electrons emitted from CsI crystals and films by Iyesaar et al.[18] of 215 Å.

By maximizing the transmission photocathode yield Y_b as given in Eqs. (8) and (10), we obtain the following expressions for the optimum thickness of insulator and metal photocathodes:
for insulators,

$$t_{opt} = \lambda_S \sinh^{-1}(\lambda_x/\lambda_S), \quad (11)$$

for metals,

$$t_{opt} = \lambda_S \ln(\lambda_x/\lambda_S). \quad (12)$$

For the insulator, cesium iodide (choosing λ_S equal to 250 Å with photon energies of 193, 525, and 2292 eV, the x-ray attenuation lengths are 3620, 5290, and 13 470 Å, respectively, and the corresponding values for the optimum thicknesses are 840, 940, and 1170 Å, respectively. For the gold photocathode (choosing λ_S equal to 40 Å[19,20]) with the same photon energies of 193, 525, and 2292 eV, the x-ray attenuation lengths are 397, 440, and 1409 Å, respectively, and the corresponding values for the optimum thicknesses are 92, 96, and 142 Å, respectively. These values are well within the experimental precision limits suggested for the optimum thicknesses by the data presented in Figs. 18 and 19 to which we have fit the predicted Y_b vs t relations given in Eqs. (7) and (10).

V. CONCLUSIONS

The secondary electron quantum yield varies with the

photon energy approximately as $E\mu(E)$ has been demonstrated here for the metals, gold, and aluminum, for the semiconductor, copper iodide, and for the insulator, cesium iodide. The primary electron yield varies less rapidly with photon energy and approximately as $E\mu^2(E)$. [$\mu(E)E^n$ with n typically between 2.5 and 3.]

The secondary electron yield for CsI is ten to one-hundred times higher than that for Au in the 0.1–10-keV region. This increased efficiency may be attributed in part to its larger escape depth (250 Å as compared to 40 Å) and to its low electron affinity. Its high quantum yield and relatively narrow secondary electron energy distribution suggest that CsI would be a very effective photocathode for sensitive time-resolved x-ray spectroscopy into the picosecond region.

A simple model for x-ray photoemission has been extended to include the effect of photocathode thickness, which does predict the photon energy dependence for the secondary and the primary electron quantum yields and the dependence of front- and back-surface secondary electron yield upon photocathode thickness. Relatively simple expressions have been derived and can be used as semiempirical equations for quantum yield and based upon the parameter, λ_s (the escape length for the corresponding semi-infinite photocathode) which may be determined experimentally from yield-versus-thickness data. The predictions of this phenomenological model are in good agreement with the experimental measurements.

ACKNOWLEDGMENTS

The authors gratefully acknowledge the invaluable assistance in this work of Robert Hockaday, Priscilla Piano, Mary Pottenger, and Murray Tester of this laboratory, Dr. Robert Day of the Los Alamos Scientific Laboratory, and Dr. Robert Kaufman of the Lawrence Livermore Laboratory. This program is supported by a grant from the Air Force Office of Scientific Research, Grant AFOSR 79-0027, and by a supplemental Department of Energy/Lawrence Livermore Laboratory, Subcontract No. 9072209.

APPENDIX: SECONDARY ELECTRON EMISSION FROM A FINITE PHOTOCATHODE: ONE-DIMENSIONAL, RANDOM-WALK ANALYSIS

Our derivation of relations (5) and (6) for the front- and back-surface photoemission from a finite x-ray photocathode is based upon a one-dimensional random-walk analysis method of Kane[16] and upon the following assumptions

(1) The number of emitted secondary electrons is proportional to the number that have transported to the emission surface by electron-phonon scattering only. Electron-electron scattering effectively drops the energy of the secondaries below that of the vacuum level.

(2) The number of electrons is negligible that have electron-phonon scattered to the surfaces and then reflect back into the photocathode volume and manage to random walk by electron-phonon scattering to these surfaces and to escape.

(3) The probabilities per unit pathlength normal to the surfaces for electron-phonon and for electron-electron scattering, a and b respectively, are constants (independent of secondary electron energy).

(4) The mean attenuation length for the x-ray photons, $(\mu\rho)^{-1}$, is very large as compared to the one-dimensional mean free paths, a^{-1} and b^{-1}, for electron-phonon and electron-electron scattering.

We would like to calculate first the probability $q(x)$, that an electron which is excited at a distance x from the front surface of a photocathode of thickness t, will reach the front surface (at $x = 0$) by electron-phonon scattering only. This may be expressed as a sum

$$q(x) = \sum_{n=0}^{\infty} p_n(x), \tag{A1}$$

in which $p_n(x)$ is the probability that the excited electron will reach the surface by a random walk of n collisions. This probability may be expressed in terms of the probability $p_{n-1}(y)$ (a path of $n-1$ collisions before reaching the surface) by the following recursive integral

$$p_n(x) = \frac{a}{2}\left[\int_0^x p_{n-1}(y)e^{-c(x-y)}dy + \int_x^t p_{n-1}(y)e^{-c(y-x)}dy\right], \tag{A2}$$

in which we are able to write explicity the probability for the excited electron to have its first electron-phonon collision in the differential dy as

$$\tfrac{1}{2}ae^{-c(x-y)}dy \quad \text{for } y < x$$

and

$$\tfrac{1}{2}ae^{-c(y-x)}dy \quad \text{for } y > x,$$

where c is the total linear cross section for secondary electron scattering, $a + b$.

In these epxressions the factor of $\frac{1}{2}$ simply accounts for the likelihood for the excited electron either to be initially heading toward a y position that is less than or greater than x. Thus the first integral in Eq. (A2) is the contribution to $p_n(x)$ of all scatterings for which the first collision is in the volume between x and the front surface, and the second integral is that for which the first collision is in the volume between x and the back surface. Using the definition for $q(x)$ in Eq. (A1) we may now rewrite Eq. (A2) as the following relation:

$$\sum_{n=1}^{\infty} p_n(x) = q(x) - p_0(x) = \frac{a}{2}\left[\int_0^x q(y)e^{-c(x-y)}dy + \int_x^t q(y)e^{-c(y-x)}dy\right], \tag{A3}$$

where p_0 is the probability that the electron may reach the front surface without scattering and is given by

$$p_0(x) = \tfrac{1}{2}e^{-cx}. \tag{A4}$$

By differentiating Eg. (A3) twice with respect to x, we obtain the differential relation

$$q''(x) - u^2q(x) = 0, \tag{A5}$$

which must have a solution of the form

$$q(x) = Ae^{ux} + Be^{-ux}. \tag{A6}$$

Here u is equal to $(c^2 - ac)^{1/2} = (b^2 + ab)^{1/2}$ and A and B are thickness dependent.

We may now obtain A and B by substituting Eq. (A6) into Eq. (A3) (which must yield the same solution for A and B for all values of x between 0 and t). For $x = 0$, we obtain the probability that an electron which is excited at the surface will be heading toward the surface and, if not reflected, will escape, viz.,

$$q(0) = A + B = \frac{a}{2}\left[\int_0^t (Ae^{uy} + Be^{-uy})e^{-cy}dy\right] + \tfrac{1}{2}. \quad \text{(A7)}$$

And, similarly, for $x = t$, we obtain the probability that an electron which is excited at the opposite surface will reach the surface at $x = 0$ and heading toward this surface, viz.,

$$q(t) = Ae^{ut} + Be^{-ut} = \frac{a}{2}\left[\int_0^t (Ae^{uy} + Be^{-uy})e^{-c(t-y)}dy\right] + \tfrac{1}{2}e^{-ct}. \quad \text{(A8)}$$

Completing the integrals in Eqs. (A7) and (A8), we then use these two equations to solve for A and B, obtaining

$$A = -c\delta/[(u + c)(e^{2ut} - \delta^2)] \quad \text{(A9)}$$

and

$$B = ce^{2ut}/[(u + c)(e^{2ut} - \delta^2)], \quad \text{(A10)}$$

where

$$\delta = (c - u)/(c + u).$$

The number of secondaries that are excited at x within a layer dx and per unit area of photocathode surface, can be written as the photon intensity I at x, multiplied by $E\mu(E)\rho dx/\bar{E}_s$ according to the simplified model description given above and discussed in more detail in Ref. 10. [$\mu(E)\rho$ is the fraction of the photons that are absorbed per unit volume and $\bar{E}_s$ is the mean energy of the secondaries.] Therefore, we may write for the x-ray photoemission from the front and back surfaces of a finite photocathode the following quantities to which Y_s and Y_b are proportional, viz., the number of secondaries heading toward and at these surfaces:

$$Y_f \sim E\mu(E)\rho\int_0^t q(x)e^{-\mu\rho x}dx, \quad \text{(A11)}$$

$$Y_b \sim E\mu(E)\rho\int_0^t q(t-x)e^{-\mu\rho x}dx. \quad \text{(A12)}$$

Finally, by substituting into these relations the expressions for A and B given in Eqs. (A9) and (A10) and making the assumption that the x-ray attenuation length $(\mu\rho)^{-1}$ is very large as compared to the escape length u^{-1}, we obtain the x-ray photoemission yields that were quoted in the text's Eqs. (5) and (6), viz.

$$Y_f = KE\mu(E)\rho\frac{c}{u(u + c)}\frac{1 - e^{-ut}}{1 + \delta e^{-ut}} \quad \text{(A13)}$$

and

$$Y_b = KE\mu(E)\rho\frac{ce^{-\mu\rho t}}{u(u + c)}\frac{1 - e^{-ut}}{1 + \delta e^{-ut}}. \quad \text{(A14)}$$

The constant K is the fraction of the electrons that are heading toward emission surface and are just inside that surface which do escape. To determine this quantity, appropriate assumptions must be made for the internal secondary electron energy distribution which then allows a determination of the number of electrons with sufficient energy to escape, i.e., of energy greater than a work function or an electron affinity. (The energy distribution is a function of such parameters as the Fermi energy and the band-gap energy.) We may use the one-dimensional analysis described here to define a corresponding isotropic three-dimensional distribution of electron velocities at the surface, conserve the transverse momentum for the escaping electron, and thereby determine the escape cone angle for an electron of a given energy. Integrating this "escape probability" over the allowed angles and energies yields the total escape fraction K. This procedure has been described in Ref. 10.

[1] J. L. Gaines and R. A. Hansen, J. Appl. Phys. 47, 3923 (1976).
[2] E. J. T. Burns and J. F. Thurston, Appl. Spectrosc. 31, 317 (1977)
[3] M. J. Bernstein and J. A. Smith, IEEE Trans. Nucl. Sci. NS-26, 1 (1979).
[4] E. B. Saloman, J. S. Pearlman, and B. L. Henke, Appl. Opt. 19, 749 (1980)
[5] R. H. Day, P. Lee, E. B. Salomon, and D. J. Nagel, IEEE International Conference on Plasma Science, Montreal, Canada 1979 (unpublished).
[6] B. L. Henke and K. Premaratne, Proceedings of the International Conference on x-ray and XUV Spectroscopy Sendai, Japan, 1978 (unpublished); Jap. J. Appl. Phys. 17, Suppl. 17-2, p. 23 (1978).
[7] B. L. Henke and M. A. Tester, *Advances in X-Ray Analysis* (Plenum, New York, 1975), Vol. 18.
[8] W. B. Herrmannsfeldt, Stanford Linear Accelerator Center, SLAC Report No. 166, 1973.
[9] B. L. Henke, J. A. Smith, and D. T. Attwood, J. Appl. Phys. 48, 1852 (1977).
[10] B. L. Henke, J. Liesegang, and S. D. Smith, Phys. Rev. B 19, 3004 (1979).
[11] G. L. Stradling, H. Medecki, R. L. Kauffman, D. T. Attwood, and B. L. Henke, Appl. Phys. Lett. 39, 782 (1980).
[12] C. J. Powell, Surf. Sci. 44, 29 (1974).
[13] C. J. Tung, J. C. Ashley, and R. H. Ritchie, Surf. Sci. 81, 427 (1979).
[14] M. S. Livingston and H. A. Bethe, Rev. Mod. Phys. 9, 263 (1937).
[15] L. Pages, E. Bertel H. Jaffre, and L. Sklavenitis, At. Data 4, 1 (1972).
[16] E. O. Kane, Phys. Rev. 147, 335 (1966).
[17] W. Pong, H. K. Nishihara, and D. Chan, J. Opt. Soc. Am. 62, 487 (1972).
[18] T. É. Ïyésaar, A. M. -É. Saar, and M. A. Élango, Sov. Phys. Solid State 20, 454 (1978).
[19] W. Pong, R. Sumida, and G. Moore, J. Appl. Phys. 41, 1869 (1970).
[20] R. E. Thomas, J. Appl. Phys. 41, 5330 (1970).

The characterization of x-ray photocathodes in the 0.1–10-keV photon energy region

B.L. Henke, J. P. Knauer,[a] and K. Premaratne
University of Hawaii, Honolulu, Hawaii 96822

(Received 25 September 1980; accepted for publication 2 December 1980)

A method and an instrument are described for the measurement of the absolute quantum yield for front-surface and transmission photocathodes in the 0.1–10-keV photon energy region. The total and the secondary electron photoemission yields have been measured for the Al, Au, CuI, and CsI photocathodes as required for the absolute calibration of the x-ray diode detectors and for the x-ray streak cameras. The relative secondary electron yields have also been measured for the same photocathodes by high resolution electron spectroscopy of the secondary electron energy distributions, which are in good agreement with the absolute yield measurements. The secondary electron yield of CsI is ten to one-hundred times higher than that for Au in the 0.1–10-keV region and with a secondary energy distribution that is appreciably sharper. For these reasons, CsI should be an effective photocathode for sensitive, time-resolved spectroscopy into the picosecond region. It is verified experimentally that the secondary electron quantum yield varies approximately as $E\mu(E)$, with E as the photon energy and $\mu(E)$ as the photoionization cross section, and that the primary (fast) electron quantum yield is a small fraction of the total yield and varies approximately as $E^2\mu(E)$. A simple model for x-ray photoemission is described which leads to semiempirical equations for front- and back-surface secondary electron photoemission as based upon an escape depth parameter that may be obtained from yield-versus-photocathode thickness data. The model predictions are in good agreement with experiment.

PACS numbers: 79.60.Cn, 79.60.Eq, 72.10. – d

I. INTRODUCTION

Time-resolved x-ray spectroscopy has become of considerable importance in the temperature density composition diagnostics of high-temperature plasmas involved in controlled thermonuclear fusion studies which utilize laser, particle beam, or magnetic compression-confinement production. The time duration of the associated x-ray emission ranges from picoseconds to seconds. Time-resolved x-ray spectroscopy is also important in the development of superradiant, pulsed x-ray sources, their application to studies of the radiation effects of x-ray bursts upon materials, and the x-ray analysis of atomic, molecular, and solid-state time-resolved processes into the picosecond region.

The electron currents that are emitted by photocathodes under x-ray excitation can be a very effective basis for time resolved spectroscopic measurement using x-ray diode or streak camera detection.[1–5] In the latter, an x-ray spectrum can be established along a slit-defined transmission photocathode of the streak camera by using focussing filter-total-reflection monochromator, crystal/multilayer arrays, or nonfocussing, Bragg reflecting crystal/multilayer analyzer systems.

In time-resolved x-ray spectroscopy, the ultimate limit on the achievable time resolution is the quantum conversion efficiency of the photocathode (which determines signal statistics) and the energy spread of the emitted electrons as is noted in Fig. 1 (which determines the time resolution).[6] The relatively small fraction of fast electrons that is photoemitted is effectively blocked by the electron optical apertures of the typical streak camera. In Fig. 2 the difference in the arrival time at the output end of the streak camera is given as a function of the energy width Δ of the secondary electron energy distribution, the extraction field ϵ_0, and of the geometry of the camera. In addition to the absolute yield-versus-photon energy and the shape of the secondary electron distribution curves, other important characteristics of the x-ray photocathode are its stability, reproducibility, simplicity of spectral response, and the linearity of its time response. Described here is a method and an instrument for the measurement of the absolute total and secondary electron yields

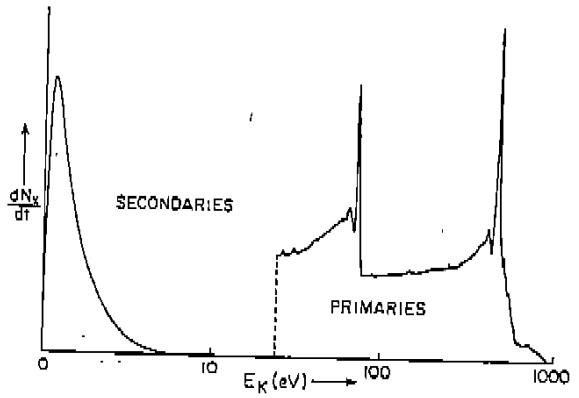

FIG. 1. In the 0.1-10-keV photon energy region the larger fraction of the electrons that are emitted are the secondary electrons, typically as a narrow distribution below 10 eV. The higher energy, fast electron photoemission consists of relatively sharp elastically scattered photoelectrons and Auger electron "lines" along with a much larger number of inelastically scattered electrons in their low-energy tail region.

[a]Present address: Lockheed, LMSC Palo Alto Research Laboratory, Org. 52-11, Building 203, 3251 Hanover Street, Palo Alto, California 94304.

 0021-8979/81/1509-12$01.10